Applied Chemical Engineering (2026) Volume 9 Issue 3 ISSN: 2578-2010 (O)
doi: 10.59429/ace.v9i3.5936

RESEARCH ARTICLE

Green Synthesis and Characterization of SiO_2/Cr_2O_3 Nanocomposites via Sol-Gel Method Using Ganoderma lucidum (Reishi Mushroom) Extract

Ameerah S. Jawad*, Abbas A-Ali Drea, Abbas Jassim Atiyah

University of Babylon, College of Science, Department of Chemistry, Babylon-Iraq

***Corresponding author:** Ameerah S. Jawad, ameerasalam900@gmail.com

ABSTRACT

This work presents a study on the green synthesis of SiO_2/Cr_2O_3 nanocomposites utilizing silica extracted from rice husk ash (RHA), and Ganoderma lucidum extract as a biogenic reducing or stabilizing agent via a modified sol–gel framework. The nanocomposites were synthesized at three SiO_2: Cr_2O_3 molar ratios (1:1, 1:2, and 2:1) and subsequently subjected to calcination at temperatures the ranging from 200°C to 600°C. Comprehensive physicochemical characterization was carried out using X-ray diffraction (XRD), Fourier-transform infrared spectroscopy (FTIR), and field emission scanning electron microscopy (FESEM), energy-dispersive X-ray spectroscopy (EDX), atomic force microscopy (AFM), and Brunauer–Emmett–Teller (BET) surface area analysis. The results showed consistent changes in morphology, crystallinity, and surface qualities. XRD studies revealed that, depending on molar ratio and calcination temperature, crystallite sizes ranging from 13.52 to 27.98 nm for pure SiO_2 and 8.31–39.77 nm for the nanocomposites. The surface area of the BET showed that the calcination at 500°C resulted in practically pure SiO_2 with a maximum specific surface area of 401.36 m^2/g. In contrast, the surface area reduced significantly, to less than 15 m^2/g, indicating the addition of Cr_2O_3, and the average pore diameter changed significantly. The findings highlight the fact that a combination of the concepts of green chemistry and advanced methods of nanomaterial production enables the synthesis of nanocomposites of SiO_2:Cr_2O_3 with tailored structural and textural characteristics. These nanocomposites can be considered as having a great potential in heterogeneous catalysis, energy storage devices and environmental remediation.

Keywords: Ganoderma lucidum, Sol–Gel Method, SiO_2/Cr_2O_3 Nanocomposites, Rice Husk Ash, Green synthesis.

ARTICLE INFO

Received: 09 March 2026
Accepted: 29 May 2026
Available online: 30 October 2026

COPYRIGHT

Copyright © 2026 by author(s).
Applied Chemical Engineering is published by Arts and Science Press Pte. Ltd. This work is licensed under the Creative Commons Attribution-NonCommercial 4.0 International License (CC BY 4.0).
https://creativecommons.org/licenses/by/4.0/

1. Introduction

Developed more effective chemical techniques while reducing environmental effect at every level of process design and implementation [1-4], green chemistry has become a vital cross-discipline framework combining ideas from synthetic chemistry, analytical chemistry, toxicology, biotechnology, and chemical engineering. Nanotechnology presents chances within this framework to create practical materials via environmentally friendly paths [3, 4].

An originally multidisciplinary discipline, nanotechnology facilitates the creation of new materials processing distinctive and beneficial characteristics[5]. Particularly because of their little size, surface effects, and quantum tunneling phenomena, nanoparticles have become quite popular and have several uses in conventional materials, medical equipment, electronic devices, coatings, and many other industries[6-8]. Their dimensionality, morphology, composition, and

origin—the latter group covering naturally occurring, accidental, bioinspired, and engineered kinds [7] can be used to categorize these nanomaterials.

With roughly 80 million tons of rice husk ash (RHA) produced globally each year [9] rice husk, an agricultural waste material, is a major and sustainable silica source. RHA often contains a major quantity of silica (up to 96.15%), along with trace elements like alumina (0.48%) and ferric oxide (0.156%)[10]. Using sol-gel or precipitation approaches, SiO_2 nanoparticles made from RHA can be sourced sustainably. So, agricultural waste is greatly reduced by removing the need for synthetic precursors like tetraethyl orthosilicate (TEOS)[11, 12].

A complex group of functional materials is represented by nanocomposites (Cr_2O_3/SiO_2) based on silicon dioxide (SiO_2), and chromium(III) oxides (Cr_2O_3). They take advantage of the unique properties of each component, SiO_2 has been widely studied due to its high chemical and thermal stability, low toxicity and ability to be functionalized at the surface in a wide range of ways [13], and Cr_2O_3 has strong magnetic, catalytic and electrochemical properties[14, 15]. The physicochemical properties of Cr_2O_3 nanoparticles were synergistically incorporated into a nanoscale structure either by dispersing Cr_2O_3 nanoparticles in a SiO_2 framework or by using core shell structures, where neither of the individual components alone could produce the same properties[15]. There has been a significant increase in interest in the Cr_2O_3/SiO_2 nanocomposites due to their future use in energy storage, catalysis, and environmental remediation.

In this work, a unified green synthesis procedure of SiO_2/Cr_2O_3 nanocomposites using RHA derived silica as the source of silica, Cr (III) as the source of Cr and the use of a biogenic stabilizer, *G. lucidum* aqueous ethanol extract to enable the formation of the final nanocomposites product. We experimentally examine the effect of molar composition (1:1, 1:2, 2:1 SiO_2/Cr_2O_3) and the temperature of calcination (200-600°C) on the structural, morphological, and textural properties of the resultant materials. The work is related to the emerging literature on bioinspired nanomaterials and illustrates the practicality of agricultural waste valorization in the framework of the circular economy framework.

2. Experimental section

2.1. Chemicals

Rice husk ash (RHA), derived from locally sourced rice husks collected in Babil region, Iraq, was used as the silica precursor. Chromium(III) nitrate nonahydrate ($Cr(NO_3)_3 \cdot 9H_2O$, analytical grade) served as the precursor for Cr^{3+} ions. The green reducing and stabilizing agent, *Ganoderma lucidum mushroom* extract, was prepared according to the procedure described below. All other chemical reagents, including sodium hydroxide (NaOH, 2.5 M), sulfuric acid (H_2SO_4, 5 M), and hydrochloric acid (HCl, 6 M), were all of analytical grade and used without further purification. Deionized water (resistivity ≥18.2 MΩ·cm) was used throughout all experimental procedures.

2.2. Methods

2.2.1. Preparation of Ganoderma lucidum Extract

Ganoderma lucidum mushrooms were procured from local markets, thoroughly washed, air-dried, and finely powdered to improve extraction efficiency. The powdered material (50 g) was subjected to maceration in 500 mL of (70:30 v/v) water-ethanol mixture at room temperature (25 ± 2°C). To prevent photo-oxidation of bioactive constituents, the mixture was transferred to dark glass containers and stored for 14 days with daily agitation (5 min per day). After the extraction period, the mixture was filtered through Whatman No. 1 filter paper to remove solid residues. The obtained filtrate showed a pH of (4.0 ± 0.2), confirming of its mildly acidic nature [16]. The filtrate was subsequently stored at 4 °C until prior to subsequent experimental applications.

2.2.2. Extraction of SiO_2 from Rice Husk Ash

Rice husks were first burnt in a muffle furnace at temperatures of 700°C and a time of four hours under stagnant air conditions to produce rice husk ash (RHA) [17]. The resulting ash 20 g was then subjected in 200 mL of a 2.5 M solution of sodium hydroxide (solid-liquid ratio 1:10w/v) and heated at 80°C under continuous stirring using magnetic stirrer at 600 rpm, which facilitated the extraction of sodium silicate (Na_2SiO_3). The alkaline extract was filtered using filter paper no. 1 Whatman in order to eliminate the insoluble residues. High-purity silica was gradually added to the filtrate, which contained the sodium silicate, under agitation to allow the silica to precipitate until the pH of the solution became 7 and maximum precipitation was achieved. The precipitate of silica thus obtained was thoroughly purified by refluxing in 6 M HCl for 2 h in order to eliminate any metallic contaminants. The product was washed with deionized water until a neutral pH was attained as shown in figure 1. The crystal-cleaned silica gel was heated to 110°C over a period of twelve hours, followed by heating at 700°C over a period of two hours to form amorphous silica oxide nanoparticles[18].



Figure 1. Schematic representation of silica extraction process from rice husk: (**A**) Raw rice husk, (**B**) Rice husk ash obtained after calcination at 700 °C, (**C**) Formation of silica gel, and (**D**) final nanosilica powder.

2.2.3. Synthesis Method for SiO_2/Cr_2O_3 Nanocomposites

The synthesis of SiO_2/Cr_2O_3 nanocomposites occurred through an adjustment of the sol-gel process. In summary, a 1 M solution of $Cr(NO_3)_3 \cdot 9H_2O$ was fully dissolved in deionized water. The aqueous silica sol was then added to this solution, and aqueous silica dispersed RHA-derived SiO_2 in deionized water was subjected to ultrasonication (30 min, 40 kHz, 150 W) to ensure even dispersion. The Ganoderma lucidum extract was subsequently added dropwise added (20mL per batch of synthesis) to the mixture, acting as both a reducing agent and also as a capping agent, which helps in the formation of chromium oxide nanoparticles and also helps in the distribution of the nanoparticles uniformly in the silica matrix[19-21].

The three molar ratios of the SiO_2 to Cr_2O_3 (1:1, 1:2 and 2:1) were systematically studied. Each of the reaction mixtures was titrated to the pH between 7.0 and 8.0 by slowly adding 2.5 M NaOH over a period of about three hours. The gelation was allowed to last two hours and the resultant gels were then dried overnight at 100 °C. The dried gels were then divided and heated in a muffle furnace at temperatures of 200, 300, 400, 500, and 600 °C, over the course of two hours using the heating rate of (5 °C min^{-1}) to determine the effect of thermal treatment on the phase formation, crystallization behavior and particle growth. All procedures of synthesis were repeated three times to achieve reproducibility and reliability of the experiment.

2.3. Characterization Techniques

The structural properties of the synthesized materials was investigated by X-ray Diffraction (XRD, using Bruker D8 Advance diffractometer, equipped with Cu-Kα radiation (λ = 0.15406 nm) operating at 40 kV with 40 mA. Diffraction data were collected over 2θ range of 10–80° with a step size of 0.02°. The average crystallite sizes were calculated from the XRD patterns using the Scherrer equation: $D = K\lambda /(\beta \cos \theta)$, where K the shape factor (0.9), β represents is the full width at half maximum (FWHM) of the different peak, and θ is the Bragg angle, λ is the X-ray wavelength [22]. Crystallite sizes was calculated from the XRD patterns by the Scherrer equation.

Fourier-transform infrared spectroscopy (FTIR, PerkinElmer Spectrum Two) was performed in the range of 400–4000 cm^{-1} with resolution of 4 cm^{-1}, and accumulated 32 scans. In order to identify characteristic chemical functional groups and bonding environments.

Surface morphology and particle size distribution was studied using Field Emission Scanning Electron Microscopy FESEM, using Zeiss GeminiSEM 300. The instrument was operated at accelerating voltages of 4-15 kV. Elemental composition and purity were verified by Energy-Dispersive X-ray Spectroscopy (EDX) coupled with the FESEM system.

The surface topography and roughness parameters was assessed using Atomic Force Microscopy (AFM, Veeco Dimension Icon), operating in tapping mode with silicon tips having a resonant frequency approx ~300 kHz, with scan rate 1 Hz. The textural properties were determined via nitrogen adsorption-desorption at 77 K using a Micromeritics ASAP 2460 surface area analyzer. Before to analysis, all samples were degassed at 200°C for 6 h under vacuum (<10 μmHg. The Specific surface areas was calculated according to the Brunauer-Emmett-Teller (BET) method within the relative pressure P/P_0 range of 0.05–0.30, while pore size distributions were determined from the Barrett-Joyner-Halenda (BJH) model applied to the desorption branch of the isotherm [23].

3. Results and Discussion

3.1. X-Ray Diffraction (XRD) Analysis

XRD analysis provided important information on the structural development and crystallinity of the prepared pure SiO_2 and SiO_2/Cr_2O_3 nanocomposites and thus, explained the interdependence between the major amorphous silica structure and the simultaneously crystallized chromium oxide nanoparticles. The diffractograms indicate that the crystallinity of the pure SiO_2 and the composite specimens is systematically increased by thermal treatment [24-26]. Figure. 2 shows the diffraction pattern of pure SiO_2 has a wide amorphous halo at $2\theta \approx 22$ which is typical of amorphous silica. The appearance of minor diffraction patterns is at high temperature, and its intensity is also monotonically increasing between 200 °C and 600°C which is a sign of progressive structural ordering. These initial peaks can be related to the first crystallization of silica phases, like cristobalite; however, the general tendencies are rather amorphous. Coherence lengths were calculated using the Scherrer equation which was synonymous to crystallite sizes in amorphous materials which were more accurate in describing the short-range ordered domains. The experimentally determined coherence lengths are monotonically dependent on the calcination temperature with a coherence length of 13.52 nm at 200°C and 27.98 nm at 600°C (**Table1**). This tendency is in accordance with the thermally absorbed structural reorganization and the overall increase in short-range ordering in silica network [13].

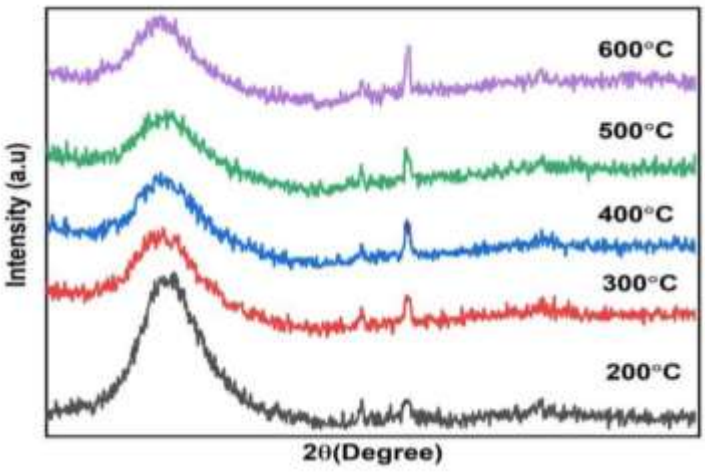


Figure 2. XRD patterns of pure SiO_2 prepared via the sol-gel method at different calcination temperatures (200 - 600 °C).

Table 1. Average crystallite size of pure SiO_2 as a function of calcination temperature.

Calcination Temperature (°C)	Average Crystallite Size (nm)
200	13.52
300	15.84
400	19.21
500	23.65
600	27.98

In the composite samples, the crystallite size of Cr_2O_3 phase was found to be strongly dependent on both the molar ratio of SiO_2 to Cr_2O_3 and the calcination temperature. For, the 1:1 ratio samples exhibited crystallite sizes ranging from 10.94 to 39.77 nm (**Table 2**). In contrast, the 1:2 and 2:1 SiO_2:Cr_2O_3 ratios, exhibited the crystallite sizes ranged from 9.67–26.51 nm and 8.31–18.44 nm, respectively (**Table 2**). Interestingly, the results indicate that the interaction between the silica matrix and the chromium oxide phase plays a critical role in controlling crystallite growth. Particularly samples with a higher silica content (2:1 ratio), tends to inhibit significant grain growth of Cr_2O_3, resulting in smaller average crystallite sizes compared to pure Cr_2O_3 reported in other literature, and also in comparison to the 1:1 ratio. The amorphous silica matrix serves as a physical barrier to prevent agglomeration, and limit Cr_2O_3 nanocrystal growth throughout thermal treatment[27, 28]. The SiO_2/ Cr_2O_3 nanocomposites demonstrated distinct diffraction patterns corresponding to the Eskolaite phase of Cr_2O_3 (JCPDS No. 38-1479, hexagonal structure, R-3c space group). Figure 3 are presents the XRD patterns for the three molar ratios across the calcination temperature range. Prominent reflections at $2\theta = 24.5°$ (012), 33.6° (104), 36.2° (110), 41.5° (113), 50.2° (024), 54.9° (116), and 63.5° (214) confirm the formation of crystalline Cr_2O_3 [28,29]. Moreover, the intensity and clarity of these diffraction peaks grew with increasing calcination temperature, showing improved crystallinity and particle development within the composite samples [29-31].

Crystallite size analysis indicates that crystallite size shows a non-monotonic, but complex relationship with composition and thermal treatment. In more specific terms, the 1:1 sample is the largest in terms of crystallites at a temperature of 200°C, and the average size of the crystallites is 39.77 nm; this is likely attributed to the increased rate of nucleation due to a balanced mixed supply of the two oxide species. The 2:1 (SiO_2-rich) formulation, on the other hand, can result in a consistently smaller size of crystallites in the order of 8.31 to 18.44 nm, which is an expression of an amorphous silica framework that effectively inhibits the spatial expansion of the Cr_2O_3 grains and interfacial development. The benefits of this isolation effect are in the applications of high surface area and many active sites, e.g. heterogeneous catalysis[32-34]. The non-

monotonic characteristic that is exhibited in all the compositions is a subject to further research as studies could be conducted by in-situ high-temperature XRD measurements to be able to explain the competing processes that control the nucleation, crystal growth, and matrix restructuring

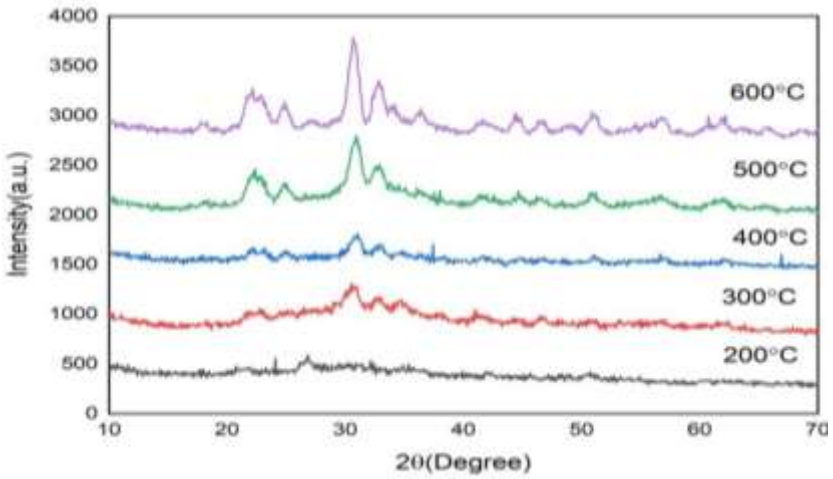


Figure 3. X-ray diffraction (XRD) patterns of SiO_2/Cr_2O_3 nanocomposites with different SiO_2:Cr_2O_3 molar ratios: 2:1, following calcination at temperatures ranging from at 200–600°C.

Table 2. Average crystallite sizes of SiO_2/Cr_2O_3 nanocomposites at different molar ratios

Calcination Temperature (°C)	Average Crystallite Size (nm) for 1:1 Ratio	Average Crystallite Size (nm) for 1:2 Ratio	Average Crystallite Size (nm) for 2:1 Ratio
200	39.77	26.50	8.75
300	11.22	26.52	17.18
400	22.01	21.49	8.31
500	10.94	9.68	15.02
600	12.45	10.58	18.44

3.2. FTIR Spectroscopy

The FTIR spectroscopy proved the efficient establishment of the oxide networks in the pure silica and the nanocomposites formed. In all the specimens, typical silica absorption bands could easily be seen (Figure 4). Si-O-Si stretching vibrations, which are pronounced (between 1000-1100 cm^{-1}, asymmetric stretching) and are accompanied by a shoulder at around 1200 cm^{-1} , are signatures of longitudinal-optical (LO) mode splitting and there is a band at approximately 800 cm^{-1}, corresponding to symmetric stretching [20, 25]. The presence of chromium oxide was unequivocally confirmed by distinct Cr–O stretching vibrations, observed at approximately 414, 451, 563, and 629 cm^{-1}, which are characteristic of the Cr_2O_3 crystalline structure. The broad band centered at 3400 cm^{-1} and the sharp peak at 1640 cm^{-1} were assigned to O–H stretching and H–O–H bending of vibration, respectively, arising from adsorbed water and surface silanol groups [35, 36].

In the SiO_2/Cr_2O_3 nanocomposites (Figure 5), the presence of chromium oxide is confirmed by characteristic Cr–O stretching vibrations at approximately 414, 451, 536, 563, and 629 cm^{-1}, which are diagnostic of the Cr_2O_3 corundum structure [25, 35] At lower calcination temperatures (200 and 300°C), additional absorption bands at ~2859 and 2924–2932 cm^{-1} are associated with residual organic matter derived from the G. lucidum extract (C–H symmetric and asymmetric stretching vibrations), along with additional bands near 1386–1419 cm^{-1} likely corresponding to C–H bending modes or intermediates generated during the decomposition of residual nitrates (NO_3^-). Above 400 °C, these organic-related bands vanish and lose intensity, therefore verifying the complete elimination of the biogenic template and perfect transition to the inorganic

oxide framework. With higher calcination temperatures, the Cr–O stretching bands likewise become increasingly sharper and show slight blue-shifts, in line with improved structural ordering and network densification of the oxide network.

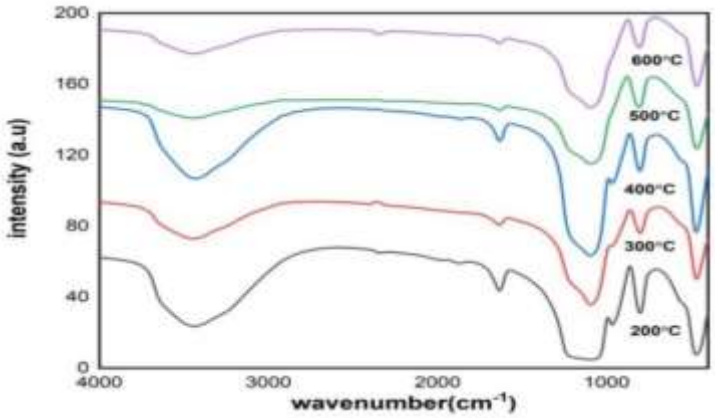


Figure 4. FTIR spectra of pure SiO_2 synthesized via the sol-gel method at calcination temperatures ranging from (200 °C to 600 °C).

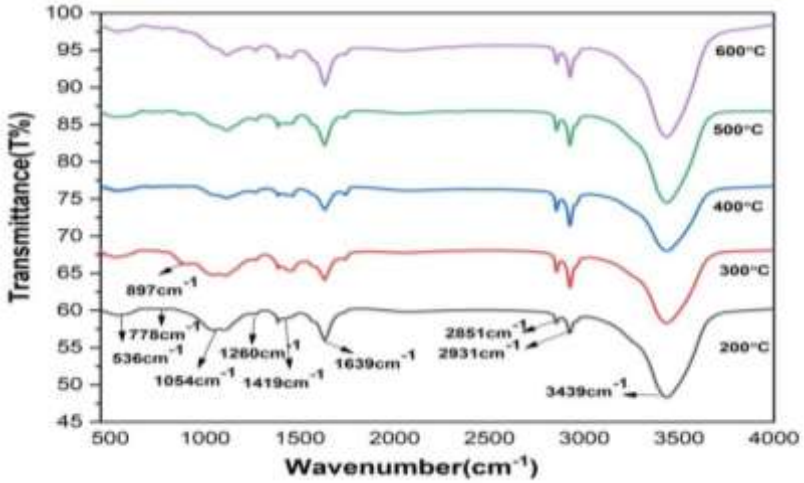


Figure 5. FTIR spectra of SiO_2/Cr_2O_3 nanocomposites prepared at different SiO_2:Cr_2O_3 molar ratios: (a) 1:1, (b) 1:2, and (c) 2:1, following calcined at temperatures ranging from (200 °C to 600 °C).

3.3. FESEM and Morphological Analysis

The field-emission scanning electron microscopy (FESEM of the synthesized nanoparticles are largely spherical though some level of agglomeration is observed, which is an attribute of high-surface-area nanoparticles. In the case of pure SiO_2 (Figure 6, Table 3), the average particle size is 59.68 nm and 36.21 nm at 200°C and 400°C, respectively, which can be explained by the removal of organic impurities and subsequent increase in silica frame density. The diameter of the particles grows significantly at high temperatures of calcination at 600°C and is in line with thermally driven processes of Ostwald ripening and sintering, wherein the particles coalesce and growth.

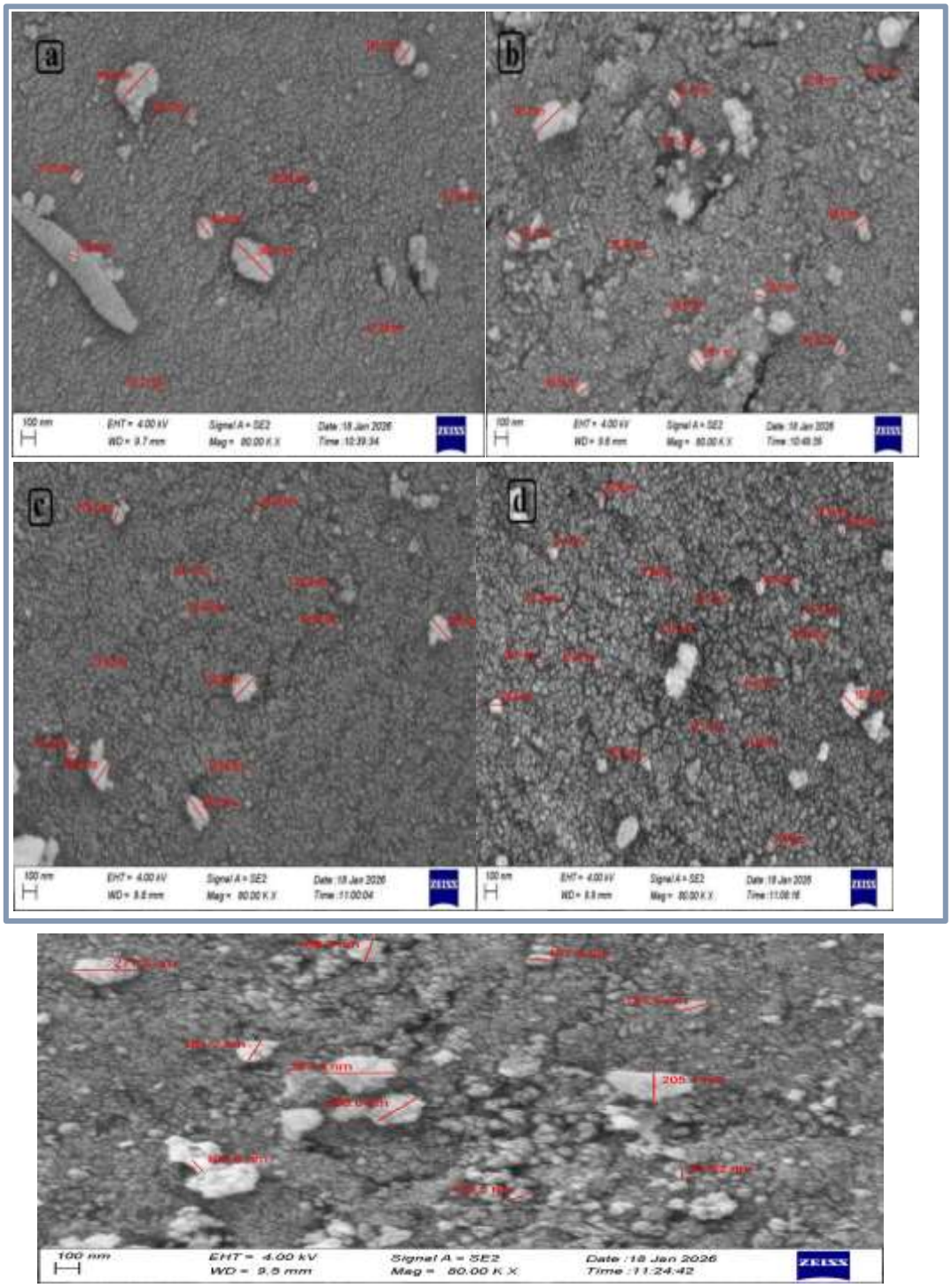


Figure 6. FESEM images of pure SiO_2 nanoparticles prepared at different calcination temperatures: (a) 200 °C, (b) 300 °C, (c) 400 °C, (d) 500 °C, and (e) 600 °C.

Table 3. Average particle size of pure SiO_2 from FESEM analysis.

Calcination Temperature (°C)	Average Particle size (nm)
200	59.68
300	43.49
400	36.21
500	39.45
600	82.11

The morphological study of nanocomposite formation reveals that the distribution of particle sizes are highly affected by the molar ratio and the calcination temperature (Figure 7, Table 4). Formulations with equimolar 1:1 ratios have average agglomeration, and the nanoparticles have dimensions of 48.03 to 68.27 nm; 1:2 ratio (Cr_2O_3-rich) samples have the largest dimensional variance of 49.31 to 82.16 nm; and 2:1 ratio (SiO_2-rich) samples have relatively uniform dimensions of 50.01 to 77.69 nm [38]. It should be noted that the XRD-derived crystallite sizes, and the FESEM-measured particle sizes are not equal measures: XRD is a scale of the sizes of coherent diffraction domains, and FESEM is a scale of the physical particle dimensions, which can have many crystalline domains within it. The relatively tight size distributions as seen through agglomeration, are indicative of the performance of the *Ganoderma lucidum* extract in terms of its use as a capping and stabilizing agent of the nanocomposite.

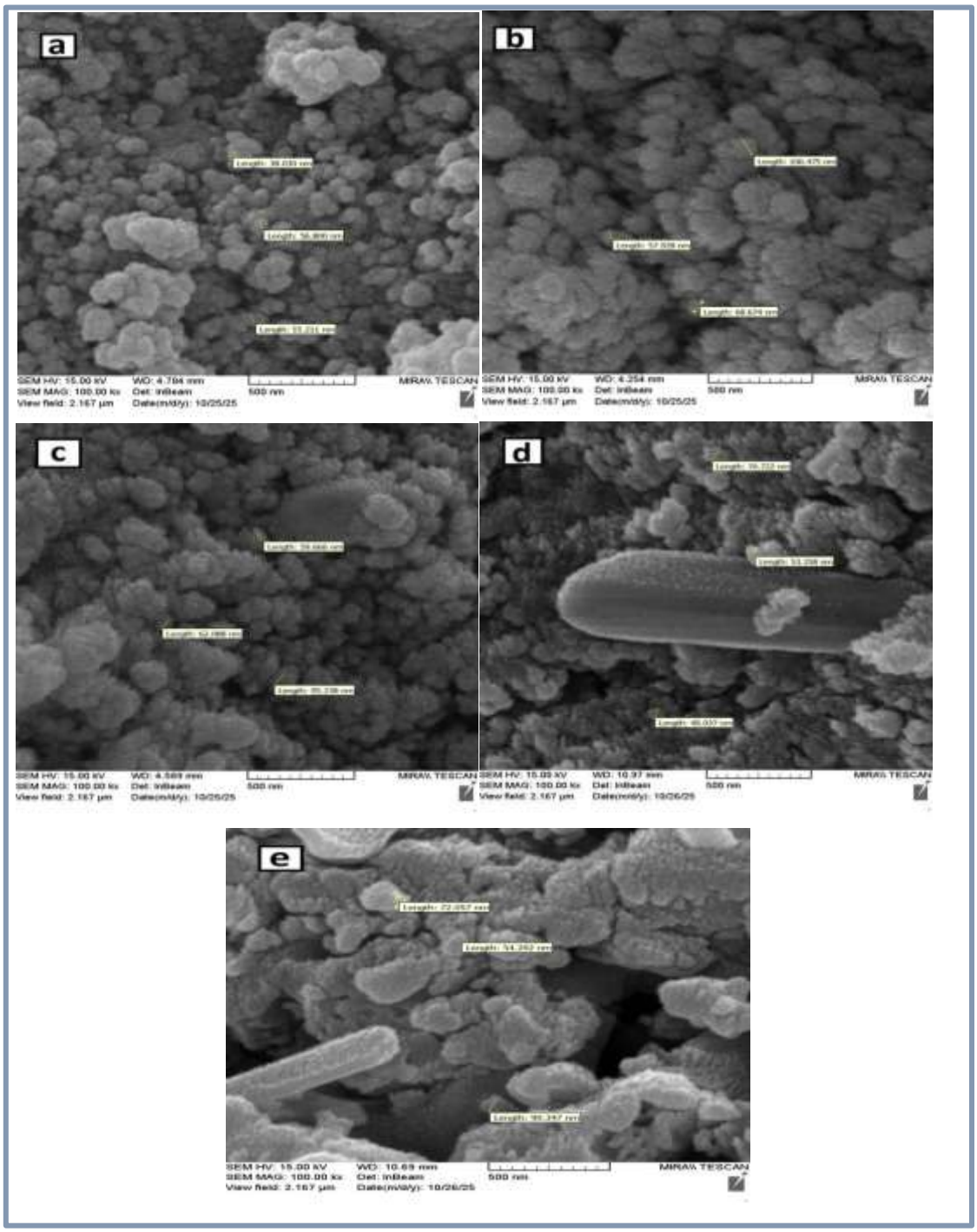


Figure 7. FESEM images of SiO_2/Cr_2O_3 nanocomposites in 2:1 molar ratio, synthesized with different calcination temperatures: (a) 200 °C, (b) 300 °C, (c) 400 °C, (d) 500 °C, and (e) 600 °C.

Table 4. Average particle sizes of SiO_2/Cr_2O_3 nanocomposites as determined from FESEM analysis.

Calcination Temperature (°C)	Average Particle Size (nm) for 1:1 Ratio	Average Particle Size (nm) for 1:2 Ratio	Average Particle Size (nm) for 2:1 Ratio
200	68.269	50.622	50.013
300	53.301	82.159	77.692
400	48.027	68.917	72.330
500	52.077	57.625	57.705
600	55.952	49.309	72.232

3.4. EDX Analysis

Quantitative evidence of the nanocomposites elemental makeup came from energy-dispersive X-ray spectroscopy (Figure 8). All spectra for all molar ratios and calcination temperatures showed typical emission lines for Si Kα (1.74 keV), Cr Kα (5.41 keV), and O Kα (0.52 keV) [37]. The high purity of the synthesized materials and the efficacy of the acid-washing purification method for RHA-derived silica were confirmed by the lack of any visible metallic impurities, including Na, S, or other elements. It should be highlighted that the stated weight percentages do not add up to 100%, which is explained by the presence of unquantified carbon generated from the conductive carbon coating used during FESEM sample preparation, as well as potential residual organic matter and at lower calcination temperatures from possibly residual organic matter. With small deviations caused by surface segregation processes and the intrinsic sampling depth constraints of EDX analysis [38], the experimentally established Cr:Si atomic ratios came close to the nominal stoichiometric ratios.

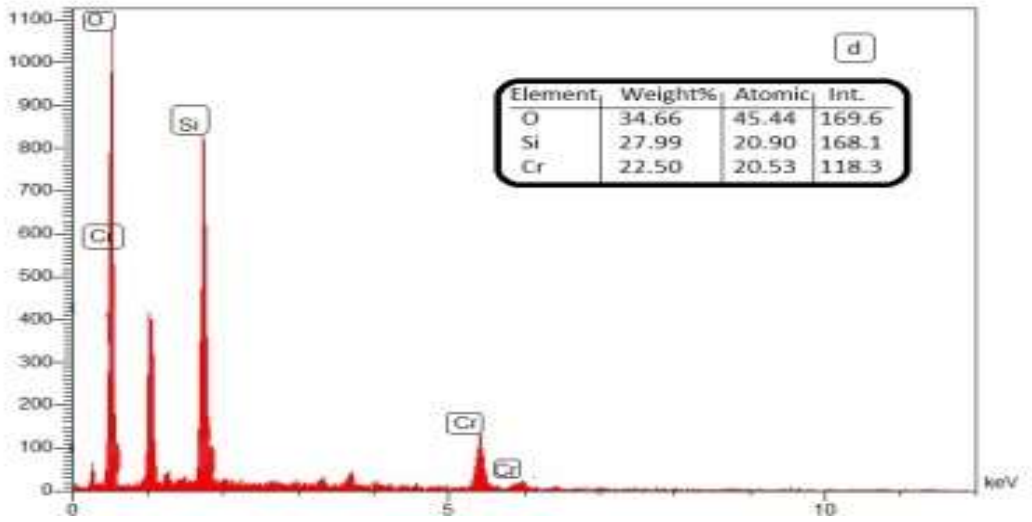


Figure 8. EDX spectra of SiO_2/Cr_2O_3 nanoparticles at a 2:1 molar ratio, calcined at d) 500 °C

3.5. AFM Analysis

Atomic force microscopy was used to describe the surface topography and roughness of the produced nanocomposites (Figure 9). Three-dimensional topographical images produced from the study confirmed the particle size measurements acquired by means of XRD and FESEM. The AFM results show nanoscale surface features with dimensions mostly matching the particle sizes calculated from FESEM and XRD for every molar ratio and calcination state.

Figure 9 shows that AFM images of the 1:1 nanocomposite that has been calcined at Cr_2O_3-rich) (**Figure 9**) gave a fairly homogeneous granular structure with a maximum height variation of about 6.6 nm in the 2D profile and about 24 nm in the 3D image [39].

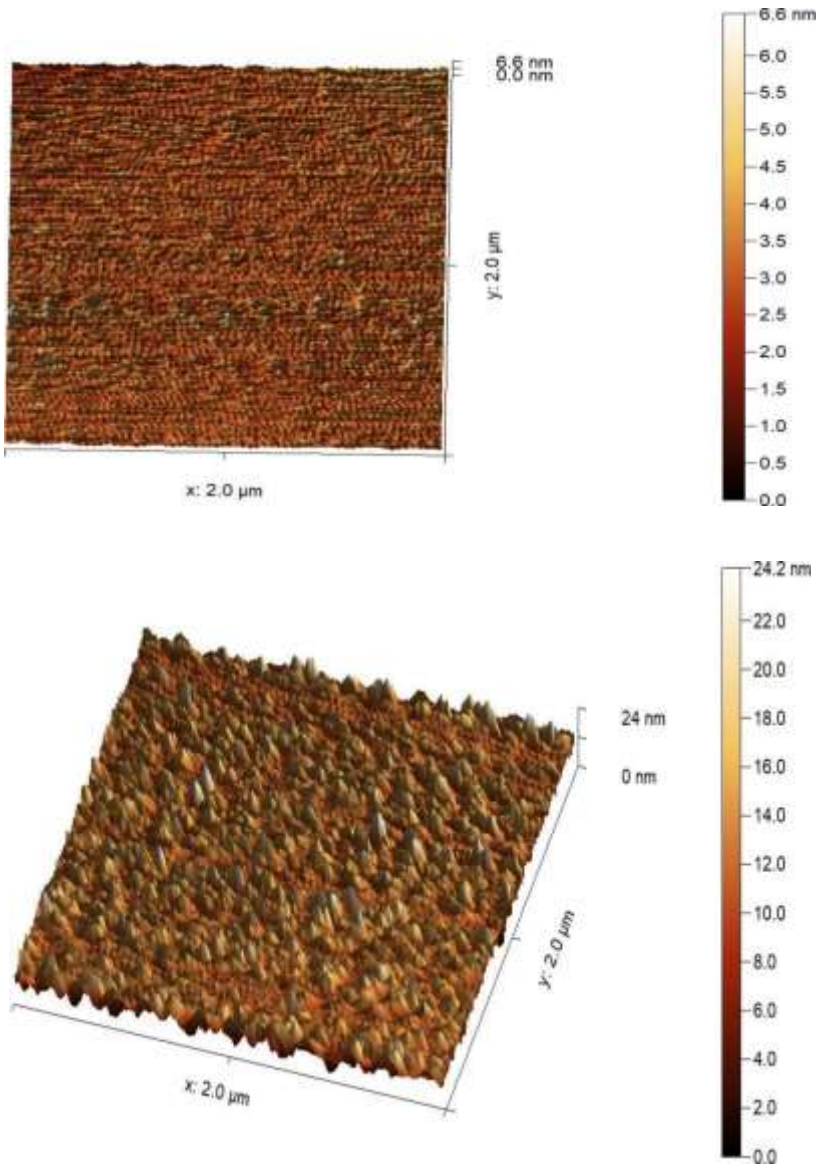


Figure 9. AFM images (2D and 3D) of SiO_2/Cr_2O_3 nanocomposites at a 1:1 molar ratio, calcined at 200 °C.

3.6. BET Surface Area and Porosity Analysis

Nitrogen adsorption–desorption measurements conducted at 77 K revealed pronounced differences in the textural properties of pure SiO_2 and the SiO_2/Cr_2O_3 nanocomposites. Characteristic of mesoporous materials with ink-bottle pore geometries [31], the Pure SiO_2 specimens showed Type IV isotherms with H2-type hysteresis loops. From 379.86 m^2/g at 200°C to a high of 401.36 m^2/g at 500°C, the BET-specific surface area rose slightly before falling slowly to 385.89 m^2/g at 600°C (Table 5). This trend indicates progressive development and stabilization of the mesoporous network with increasing thermal treatment up to 500°C, while followed by the onset of pore collapse or sintering effects at 600°C. However, the mean pore diameter remained narrowly distributed between 6.43 and 6.94 nm across the entire temperatures range, indicating the preservation of a well-defined and thermally stable mesoporous structure.

Table 5: BET surface parameters of pure SiO_2 nanoparticles as a function of calcination temperature.

Calcination Temperature (°C)	BET Surface Area (m^2/g)	Pore Volume ($cm^3\ g^{-1}$)	Mean Pore Diameter (nm)
200	379.86	0.658	6.94
300	381.99	0.662	6.94
400	391.84	0.666	6.80
500	401.36	0.667	6.64
600	385.89	0.621	6.43

Based on, the pure SiO_2, The SiO_2/Cr_2O_3 nanocomposites exhibited a pronounced reduction in specific surface areas across all compositions and calcination temperatures. For the 1:2 (Cr_2O_3-rich) ratio (**Table 6**), the BET surface areas ranged from 0.33 to 15.78 m^2/g, representing a reduction of more than 95% relative to pure SiO_2. Also, the 2:1 (SiO_2-rich) ratio (**Table 7**), similarly exhibited low surface areas in the range of 0.77–8.39 m^2/g as shown in figures 10 and 11. This reduction was accompanied by an increase pore diameters up to 38.68 nm for the 1:2 ratio (at 300°C) and reach higher as 85.58 nm for the 2:1 ratio at 600°C), in contrast sharply with the narrowly distributed mesopores (6–7 nm) observed for pure SiO_2.

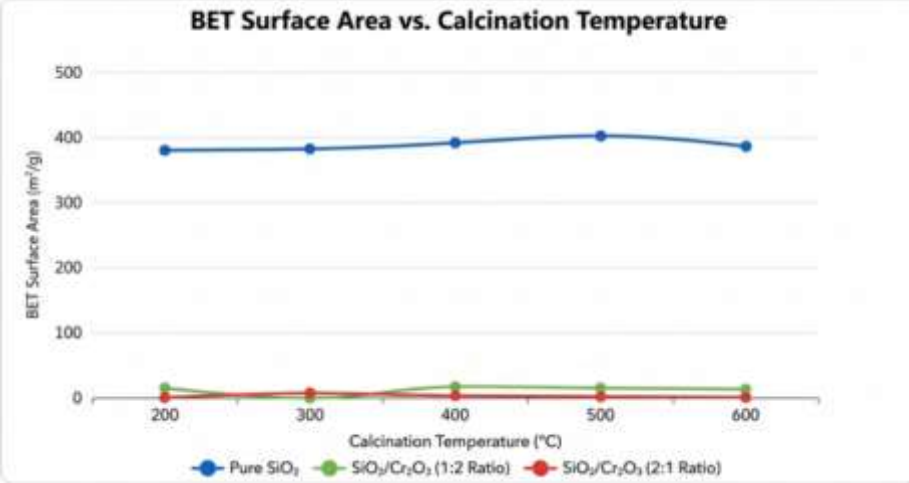


Figure 10. Comparative analysis of BET surface area for pure SiO_2 and SiO_2/Cr_2O_3 nanocomposites (1:2 and 2:1 ratios) as function of calcination temperatures.

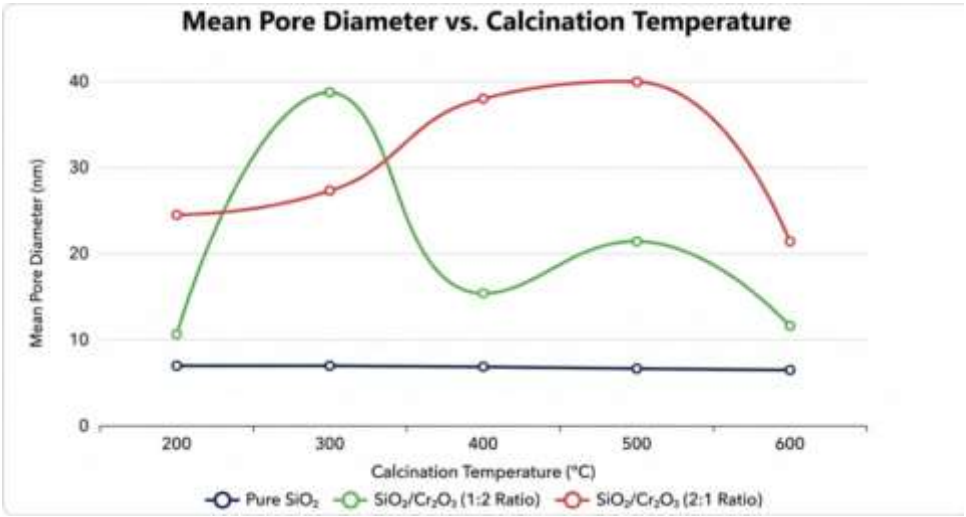


Figure 11. Comparative analysis of mean pore diameter for pure SiO_2 and SiO_2/Cr_2O_3 nanocomposites (1:2 and 2:1 ratios) as function of calcination temperatures.

This phenomenon strongly suggests that highly crystalline Cr_2O_3 nanoparticles either occupy or obstruct the mesopores of the initially high-surface-area silica matrix. The higher calcification temperatures required to form the Cr_2O_3 crystallised might cause a rearrangement or partial breakdown of the relative fragile porous silica structure to form a mixed oxide system with significantly less internal surface. The high enhancement in the mean pore diameter is a strong indication of a shift in the structure to interparticle-dominated macroporous structure. It is notable that the sample synthesized at 300°C under of 1: 2 ratio has an insignificant BET surface area of m^2/g minus and this is indicative of a critical loading of Cr_2O_3 leading to the almost complete occlusion of mesopores structure. Such as unusual phenomenon should be investigated systematically to understand the structural mechanism responsible for this behavior. The macroporous materials of this type can be especially useful in systems that involve mass transport efficiency, as in a heterogeneous catalytic or adsorption system, in which the diffusion constraints are a major consideration40

Table 6. BET surface characteristics of SiO_2/Cr_2O_3 nanocomposite (1:2 molar ratio) as a function of calcination temperature.

Calcination Temperature (°C)	BET Surface Area (m^2/g)	Pore Volume ($cm^3\ g^{-1}$)	Mean Pore Diameter (nm)
200	14.51	0.038	10.53
300	0.33	0.003	38.68
400	15.78	0.061	15.36
500	14.83	0.079	21.38
600	13.25	0.038	11.53

Table 7. BET surface characteristics of SiO_2/Cr_2O_3 nanocomposite (2:1 molar ratio) as a function of calcination temperature.

Calcination Temperature (°C)	BET Surface Area (m^2/g)	Pore Volume ($cm^3\ g^{-1}$)	Mean Pore Diameter (nm)
200	0.97	0.006	24.48
300	6.47	0.047	27.26
400	8.39	0.063	30.22
500	5.45	0.069	50.97
600	0.77	0.011	85.58

5. Conclusions

This work illustrates the effective green synthesis of the SiO_2/Cr_2O_3 nanocomposites through a modified sol gel method in which rice husk ash silica and Ganoderma lucidum extract are used as biogenic stabilizing and capping reagents. The suggested approach encourages the up-cycling of agricultural waste and eliminates the use of dangerous chemical reducing substances, which is consistent with the main principles of green chemistry and sustainable material design. comprehensive physicochemical characterisation, such as X-ray diffraction (XRD), fourier transform infrared spectroscopy (FTIR), field emission scanning electron microscopy (FESEM), energy dispersive X ray spectroscopy (EDX), atomic force microscopy (AFM) and Brunauer Emmett Teller (BET) surface area analysis confirmed the successful formation of the nanocomposites and the structural, morphological and textural characteristics of the nanocomposites are systematically adjustable by varying compositions and control of the calcination temperature.

The ratio of SiO_2: Cr_2O_3 precursor and the temperature of calcination had a strong effect on crystallinity, particle size, surface morphology as well as porosity. The silica was found to be pure and it had a large specific surface area and a distinct mesoporous structure. Conversely, addition of Cr_2O_3 caused a significant reduction in the surface area and an increment in the mean pore diameter that indicated a partial pore blockage and densification of the silica structure as a result of the Cr_2O_3 crystallization. The SiO_2 rich mix (2:1 molar ratio),

especially at the middle calcination temperature (400-500°C) offered a good balance between controlled crystallites growth and the maintenance of a relatively high surface area, thus being specifically useful in catalysis. In contrast, the more appropriate system to use could be the one with a higher pore diameter, which is (Cr_2O_3-rich) system (1: 2 molar ratio) in case a process that necessitates increased mass transport is involved.

The presented tunability of both structural and textural properties highlights the potential of such SiO_2/ Cr_2O_3 nanocomposites in high-technological application, such as heterogeneous catalysis, energy-storing systems and environmental remediation. In general, the results support the incorporation of sustainable green-chemistry concepts into the state-of-the-art nanomaterial-engineering approaches. The simultaneous valorization of agricultural waste and bio-based stabilization provides an environmentally friendly, cost efficient, and scalable platform in the synthesis of useful metal-oxide nanocomposites. This method also demonstrates how the principles of the circular-economy can be applied to the process of nanomaterials production, thus helping not only to promote industrial progress but also to ensure the sustainability of the environment.

References

1. Shafey, A., Green synthesis of metal and metal oxide nanoparticles from plant leaf extracts and their applications: A review. Green Processing and Synthesis 2020, 9, 304-339.
2. Singh, N. B., Chapter 12 - Green synthesis of nanomaterials. In Handbook of Microbial Nanotechnology, Hussain, C. M., Ed. Academic Press: 2022; pp 225-254.
3. Soltys, L.; Olkhovyy, O.; Tatarchuk, T.; Naushad, M. Green Synthesis of Metal and Metal Oxide Nanoparticles: Principles of Green Chemistry and Raw Materials Magnetochemistry [Online], 2021, p. 145.
4. Kumar, J. A.; Krithiga, T.; Manigandan, S.; Sathish, S.; Renita, A. A.; Prakash, P.; Prasad, B. S. N.; Kumar, T. R. P.; Rajasimman, M.; Hosseini-Bandegharaei, A.; Prabu, D.; Crispin, S., A focus to green synthesis of metal/metal based oxide nanoparticles: Various mechanisms and applications towards ecological approach. Journal of Cleaner Production 2021, 324, 129198.
5. Sabeti, N.; Hodhodi, A.; Rostamzad, H., Application of nanotechnology in the food industry- A review. 2023.
6. Wu, Q.; Miao, W.-s.; Zhang, Y.-d.; Gao, H.-j.; Hui, D., Mechanical properties of nanomaterials: A review. 2020, 9 (1), 259-273.
7. Barhoum, A.; García-Betancourt, M. L.; Jeevanandam, J.; Hussien, E. A.; Mekkawy, S. A.; Mostafa, M.; Omran, M. M.; S. Abdalla, M.; Bechelany, M. Review on Natural, Incidental, Bioinspired, and Engineered Nanomaterials: History, Definitions, Classifications, Synthesis, Properties, Market, Toxicities, Risks, and Regulations Nanomaterials [Online], 2022, p. 177.
8. Sune, N.; Jumde, K.; Hatwar, P.; Bakal, R.; More, S.; Korde, A., Nanoparticles: classification, types and applications: a comprehensive review. GSC Biol Pharm Sci 29 (3): 190–197. 2024.
9. Nguyen-Tri, P.; Nguyen, T. A.; Carriere, P.; Ngo Xuan, C., Nanocomposite Coatings: Preparation, Characterization, Properties, and Applications. International Journal of Corrosion 2018, 2018 (1), 4749501.
10. Adam, J. A.; Oboh, I. O.; Etuk, V. E.; Okon, F. E.; Asangausung, P. E., Extraction of silica from rice husk for the production and optimization of metallurgical-grade silicon for potential engineering applications. 2025.
11. Nguyen, T. H.; Vu, T. C.; Le, T. P.; Nguyen, T. H.; Do, X. T.; Vu, A.-T., Synthesis of Mesoporous ZnO•SiO2 Nanocomposite from Rice Husk for Enhanced Degradation of Organic Substances Including Janus Green B under Visible Light. 2024 2024, 13.
12. Ghamarpoor, R.; Fallah, A.; Jamshidi, M., A Review of Synthesis Methods, Modifications, and Mechanisms of ZnO/TiO2-Based Photocatalysts for Photodegradation of Contaminants. ACS Omega 2024, 9 (24), 25457-25492.
13. Hasanien, Y. A.; Mosleh, M. A.; Abdel-Razek, A. S.; El-Sayyad, G. S.; El-Hakim, E. H.; Borai, E. H., Green synthesis of SiO2 nanoparticles from Egyptian white sand using submerged and solid-state culture of fungi. Biomass Conversion and Biorefinery 2024, 14 (20), 26159-26172.
14. Elanssary, E. H.; Ali, I. M.; Elamin, A. A., Advances in Cr_2O_3-Based Nanomaterials: Synthesis Strategies, Functional Properties, and Sustainable Technologies. Aswan Science and Technology Bulletin 2025, 3 (2), 139-189.
15. Samuel, A.; Abdullah, A.; Xavier, G.; Stephen, S.; Zeidan, M. M.; Choi, D.; Abedrabbo, S., Sol–gel synthesis and characterization of ZnO–SiO2 nanocomposites: a comparative study with pure ZnO and SiO2. Nanoscale Advances 2025, 7 (22), 7145-7155.
16. Kareem, H. J.; Al-Araji, A. M., A Review of Ganoderma lucidum Active Compounds and their Biological Applications. Journal of University of Anbar for Pure Science 2025, 19 (1).

17. Azza Walaaldeen, K.; Huda jaafar, n.; Ghassan Abdul-Hamid, N., A Comprehensive Review of Rice Husk Derived Silica As Nano Filler (A review of literature). (Humanities, social and applied sciences) Misan Journal of Academic Studies 2025, 24 (53).
18. Al-Hussin, A. Q.; Al-gubury, H. Y.; Bader, A. T., Factors Influencing the Enhanced Photocatalytic Degradation of Congo Red Dye Using SiO2/ZnO Nanocomposite Under UV Irradiation. Journal of Nanostructures 2026, 16 (1), 517-530.
19. Khan, S. A.; Shahid, S.; Hanif, S.; Almoallim, H. S.; Alharbi, S. A.; Sellami, H. Green Synthesis of Chromium Oxide Nanoparticles for Antibacterial, Antioxidant Anticancer, and Biocompatibility Activities International Journal of Molecular Sciences [Online], 2021, p. 502.
20. Can, A.; Kızılbey, K. Green Synthesis of ZnO Nanoparticles via Ganoderma Lucidum Extract: Structural and Functional Analysis in Polymer Composites Gels [Online], 2024, p. 576.
21. Smirnov, O.; Dzhagan, V.; Kovalenko, M.; Gudymenko, O.; Dzhagan, V.; Mazur, N.; Isaieva, O.; Maksimenko, Z.; Kondratenko, S.; Skoryk, M.; Yukhymchuk, V., ZnO and Ag NP-decorated ZnO nanoflowers: green synthesis using Ganoderma lucidum aqueous extract and characterization. RSC Advances 2023, 13 (1), 756-763.
22. Paterson, R. R. M., Ganoderma – A therapeutic fungal biofactory. Phytochemistry 2006, 67 (18), 1985-2001.
23. Iravani, S., Green synthesis of metal nanoparticles using plants. Green Chemistry 2011, 13 (10), 2638-2650.
24. Rasheed, R.; Easa, H.; Sami, L., Preparation and characterization of Cr2O3 nanoparticle prepared by chemical method. 2020; Vol. 2213, p 020202.
25. Rahimzadeh, C. Y.; Barzinjy, A. A.; Mohammed, A. S.; Hamad, S. M., Green synthesis of SiO2 nanoparticles from Rhus coriaria L. extract: Comparison with chemically synthesized SiO2 nanoparticles. PLOS ONE 2022, 17 (8), e0268184.
26. Sone, B.; Elayaperumal, M.; Gurib-Fakim, A.; Maaza, M., Single-phase α-Cr2O3 nanoparticles' green synthesis using Callistemon viminalis' red flower extract. Green Chemistry Letters and Reviews 2016, 9, 85-90.
27. Tsegay, M.; Gebretinsae, H.; Nuru, Z. Y., Structural and optical properties of green synthesized Cr2O3 nanoparticles. Materials Today: Proceedings 2020, 36.
28. Klug, H. P.; Alexander, L. E., X-Ray Diffraction Procedures: For Polycrystalline and Amorphous Materials, 2nd Edition. 1974; p 992.
29. Lowell, S.; Shields, J.; Thomas, M.; Thommes, M., Characterization of Porous Solids and Powders: Surface Area, Pore Size and Density. 2006; Vol. 1.
30. Elizondo-Villarreal, N.; Gandara-Martínez, E.; García-Méndez, M.; Gracia-Pinilla, M.; Guzmán-Hernández, A. M.; Castaño, V. M.; Gómez-Rodríguez, C. Synthesis and Characterization of SiO2 Nanoparticles for Application as Nanoadsorbent to Clean Wastewater Coatings [Online], 2024, p. 919.
31. Baloria, V.; Singh, A.; Debnath, A.; Mahajan, A.; Bedi, R.; Aswal, D.; Gupta, S., Synthesis And Characterization Of Sol-Gel Derived Cr2O3 Nanoparticles. AIP Conference Proceedings 2012, 1447, 341-342.
32. Corma, A., From Microporous to Mesoporous Molecular Sieve Materials and Their Use in Catalysis. Chemical Reviews 1997, 97 (6), 2373-2420.
33. Karwa, A. S.; Gaikwad, S.; Rai, M. K., Mycosynthesis of silver nanoparticles using Lingzhi or Reishi medicinal mushroom, Ganoderma lucidum (W. Curt.: Fr.) P. Karst. and their role as antimicrobials and antibiotic activity enhancers. International journal of medicinal mushrooms 2011, 13 (5).
34. Brinker, C. J.; Scherer, G. W., Sol-gel science: the physics and chemistry of sol-gel processing. Gulf Professional Publishing: 1990.
35. Yuan, X.; Chao, Y.-J.; Ma, Z.-F.; Deng, X., Preparation and characterization of carbon xerogel (CX) and CX–SiO composite as anode material for lithium-ion battery. Electrochemistry Communications - ELECTROCHEM COMMUN 2007, 9, 2591-2595.
36. West, J.; Hench, L., The sol-gel process. Chem. Rev 1990, 90 (1), 33-72.
37. Larry, L. H.; West, J. K., The sol-gel process. Chem. Rev 1990, 90 (1), 33-72.
38. Goldstein, J. I.; Newbury, D. E.; Michael, J. R.; Ritchie, N. W.; Scott, J. H. J.; Joy, D. C., Scanning electron microscopy and X-ray microanalysis. springer: 2017.
39. Sing, K. S., J. Rouqerol and T. Siemieniewska. Pure Appl. Chem. 1985, 57, 603.
40. Alshammari, M.; Alshammari, K.; Alhassan, S.; Alshammari, A. H.; Alotaibi, T.; Alotibi, S.; Ismael, A.; Taha, T. A. M., A High-Performance Cr2O3/CaCO3 Nanocomposite Catalyst for Rapid Hydrogen Generation from NaBH4. Nanomaterials 2024, 14 (4), 333.